Results in Engineering 9 (2021) 100190

Contents lists available at ScienceDirect

Results in Engineering

journal homepage: www.editorialmanager.com/rineng/Default.aspx

Prediction of the business jet Global 7500 wing deformed shape using fiber Bragg gratings and neural network

T. Klotz [a,*], R. Pothier [b], D. Walch [c], T. Colombo [d]

[a] Aviation Systems Development and Integration, Centre Technologique en Aérospatiale (CTA), QC, J3Y 8Y9, Saint-Hubert, Canada
[b] Experimental Department, Bombardier Aviation, QC, H3C 1K3, Saint-Laurent, Canada
[c] Core Engineering, Bombardier Aviation, QC, H9P 1A2, Dorval, Canada
[d] Load and Dynamics, Bombardier Aviation, QC, H9P 1A2, Dorval, Canada

ARTICLE INFO

Keywords:
Wing deflection
Wing twist
Optical fiber
Bragg gratings
Strain measurements
Neural network

ABSTRACT

To develop a common deflection and twist measuring method applicable for both ground and flight tests, the left wing of a Global 7500 business jet was instrumented with fiber Bragg gratings and underwent durability and damage tolerance certification testing. This fiber optical sensing system allows distributed strain measurements on the wing. Fatigue and static tests were monitored. It was shown that the front and rear spar deflections could be analytically calculated with an acceptable accuracy. However, the twist could not be successfully calculated. A neural network was then used to address this issue. Even though the deflection predictions were less accurate than those analytically calculated, the wing twist was successfully predicted. This study shows the potential of using fiber Bragg grating as a shared ground and flight tests strain measuring method allowing to calculate the aircraft wing deflection and to determine the wing twist angle using a neural network.

1. Introduction

Aeronautical engineers use structural numerical models and ground tests on representative aircraft structures to optimize new wing designs. The load cases applied on both the numerical models and the ground tested structures must be as close as possible to the ones that the aircraft will encounter in-flight. For this reason, using the same measurement methods during flight and ground tests will allow to ensure that the applied load cases are properly defined.

Wing deflection and twist angle measurement is relatively straightforward when tests are performed on the ground. Different types of sensors such as vertical transducers, inclinometers and strain gauges can be used. However, these sensors are not adequate for flight test campaigns due to their weight, size, wiring and absence of ground reference. Optical observation techniques such as photogrammetry [1,2] or interferometry [3] can be used. However, during flight tests, the field of view can be limited and perturbations such as the lack of visibility due to weather conditions or aircraft window deformations resulting from cabin pressurization may compromise accurate measurements.

Following the crash, in June 2003, of the unmanned solar powered prototype aircraft Helios [4], the National Aeronautics and Space Administration (NASA) started to develop the use of fiber optic sensing systems to monitor the in-flight aircraft wings deformation and health. The fiber optic sensing systems, made of Fiber Bragg Gratings (FBG), are optical fibers in which gratings were written using ultraviolet rays. These gratings reflect, according to Bragg's law [5], a light signal having a wavelength which depends on the distance between the gratings. Hence, when a FBG is bonded on a structure, the distance between the gratings will vary evenly with the deformation of the structure and the variation of the reflected wavelength can be used as a strain measurement using the equation [6]

$$\varepsilon = \frac{\lambda - \lambda_{ref}}{\lambda_{ref}} \frac{1}{k} \tag{1}$$

in which ε represents the measured strain, λ is the reflected wavelength, λ_{ref} is the reflected wavelength at a zero-strain state and k is the FBG gauge factor. Equation (1) is valid when the temperature is constant. In case of temperature variation, temperature dependent terms can be added [6]. When gratings are distributed all along the FBG, continuous strain measurements can be acquired. For more technical information on this technology the extensive literature review performed by Ma and

* Corresponding author.
E-mail addresses: thierry.klotz@ena.ca (T. Klotz), robert.pothier@aero.bombardier.com (R. Pothier), denis.walch@aero.bombardier.com (D. Walch), tony.colombo@aero.bombardier.com (T. Colombo).

https://doi.org/10.1016/j.rineng.2020.100190
Received 22 October 2020; Accepted 19 November 2020

Abbreviations

FBG	Fiber Bragg Gratings
FEM	Finite Element Model
DADTT	Durability and Damage Tolerance Testing
RST	Residual Strength Test
ε	strain
λ	wave length
λ_{ref}	reference wave length
FBG	fiber Bragg gratings
k	FBG gauge factor
Δl	distance between two FBG strain measurements
n	total number of gratings
i	specifies the number of the strain measurement. It can be used as a subscript
x	coordinate along the FBG
C	distance between the FBG and the neutral axis
C_{top}	distance between the FBG on the upper skin and the neutral axis
C_{bottom}	distance between the FBG on the lower skin and the neutral axis
ε_{top}	upper skin strain
ε_{bottom}	lower skin strain
h	wing thickness
y	deflection
θ	spanwise angle
φ	twist angle
$y_{leadingedge}$	leading edge deflection
$y_{trailingedge}$	trailing edge deflection
d	distance between the leading and trailing edges
κ	curvature
L	beam length
E	Young modulus
D	applied displacement
I_Z	axis beam cross section area moment of inertia
X	coordinate along the beam
M_Z	axis bending moment
ε_{theory}	strain calculated using the beam theory
ε_{FEM}	strain obtained using the FEM
$\varepsilon_{FEM,approx}$	approximation of ε_{FEM}
a, b ε_{FEM}	fitting parameters
y_{theory}	deflection calculated using the beam theory
P	applied force
$y_{FEMerror}$	deflection percentage error
y_{FEM}	deflection obtained using the FEM
y_{pred}	predicted deflection
ε_{error}	relative strain error
ε_{SG}	strain measured using a strain gauge
$\varepsilon_{SG,max}$	maximum strain measured using strain gauges
ε_{FBG}	strain measured using FBG
ε_{norm}	normalized strain
WS_{norm}	normalized wing span
WS_{pos}	position on the wing span
WS_{max}	span at wing tip.
y_{norm}	normalized deflection
y_{max}	maximum deflection
y_{error}	deflection relative error
y_{PT}	measured deflection
$\Delta\theta$	spanwise angle relative error
θ_{pred}	predicted spanwise angle
θ_{INC6}	spanwise angle measured by INC6
φ_{norm}	normalized twist angle
φ_{max}	maximum twist angle
$\Delta\varphi$	twist angle error
φ_{pred}	predicted twist angle
φ_{INC}	measured twist angle

Chen [7] can be consulted. The FBG may be adequate for flight tests due to their light weight, negligible diameter ($\approx$ 0.2 mm) and their continuous strain measurement capabilities. Moreover, the FBG can be embedded in composite wings [8] and can be used for structural health monitoring [9–11]. The FBG main disadvantage is that it can only measure unidirectional strain oriented along the fiber.

In 2007, Ko et al. [12] developed a patented [13] analytical model allowing calculation of the wing deflection by measuring the span wise strain distribution using FBG [14]. This model, commonly called the Ko theory in the literature, is iterative and based on the beam theory. Jutte et al. [2] used the Ko theory to calculate the deflection of a 53 m span wing with a $\pm$ 69 mm error on a maximum wing tip deflection of 2.9 m. The Ko theory was then successfully re-tested on a 1.3 m aluminum plate by Bakalyar and Jutte [15] and Derkevorkian et al. [16], and on a 5.5 m span composite wing by Nicolas et al. [17]. The beam theory was also used by Li et al. [18] to compute the deflection of a wing spar using multiple FBG rosettes. Meng et al. [19] reported that the Ko theory is not suitable for structures submitted to large deformation and they developed another analytical deformed shape calculation model, herein referred as Meng's model, based on the curvature and successfully applied it, using FBG, on a 1 m span metallic wing. Yi et al. [20] also used the curvature to compute the deformed shape of a 380 mm epoxy resin plate.

The wing twist angle could theoretically be calculated from the deflection difference between the leading and the trailing edges using trigonometry. However, Jutte et al. [2] obtained large twist angle errors as high as 6°. As they reported, even with a good accuracy on the deflection calculations, a small error on the computed deflections leads to a large error on the calculated twist angle.

Another method based on the inverse Finite Element Method (iFEM) was developed by Tessler and Spangler [21] using their previous work on least-squares variational formulation [22,23]. The strain measured on the structure are implemented in a Finite Element Model (FEM) that computes the deformed shape of the structure. This method was successfully used by Vazques et al. [24] to calculate the deflection of a 1.2 m aluminum bar and by Song and Liang [25] to predict the dynamic displacement of beam structures. Gherlone et al. [26] found this method to be more accurate than the Ko theory. However, as previously reported by Gherlone et al. [27], this efficient method is still to adapt to real aircraft structures that have complex geometries and loading. Although FBG can provide a fine discretization of strain measurements, the FEM of an aicraft's wing is complex and computationally costly, which is a barrier to the use of this method, especially when a large number of load cases are applied on the wing.

The deflection of a structure can also be deducted from the comparison between the results of a FEM and the experimentally measured strain. The efficiency of this method was proven by Murayama et al. [28] on a 6 m composite wing box and by Cui et al. [29] on an airfoil for which the span was not reported. This method could be adapted to a real scale large airplane's wing to calculate the deflection and the twist. However, the relations between the measured strain and the wing deformation would be complex to determine.

Neural Network (NN) is a method that can create complex correlations between input parameters. It can produce results that would be impossible to obtain analytically. Nguyen et al. [30] predicted the bending and torsional moments in a 25.7 m span wing virtually

submitted to atmospheric turbulence with an error inferior to 5%. They reported that the results could be obtained instantaneously when compared to the numerical program commonly used that can run for hours. However, they also reported that the NN accuracy was much lower for atmospheric turbulence with gust velocities higher than the ones it was trained with. It is a drawback of the NN method: the NN has to be trained with a data set having the same parameter ranges than those it will face. Wada and Tamayama [31] used a NN on a 3.6 m span wing tested in a wind tunnel. The wing was equipped with FBGs. They showed that it was possible to predict the angle of attack and the distributed lift load along the span with error ranges from −1.03 to 0.46° and from −1.5 to 1.4 N, respectively. NN can also be used to calculate deflections. Kaczmarek and Szymańska [32] used it to calculate the deflection of reinforced concrete beams. They reported that the calculated deflections were more accurate than those calculated according to the standards commonly used in civil engineering. The NN would be worth trying to address the issue of the wing twist angle calculation.

The Global 7500, developed by Bombardier Aviation, is the largest and longest range business jet in the world. Equipped with new transonic wings, it can reach cruise speeds as high as Mach 0.90 [33]. Transport Canada delivered its type certificate in 2018. A complete representative structure of the Global 7500 was still under Durability And Damage Tolerance Testing (DADTT) until January 2020. The DADTT test rig has already been described by Beltempo et al. [34]. The Global 7500 representative structure's left wing was instrumented with FBGs to calculate its deflection and twist angle, with the long-term objective to develop a unified measuring method of the wing deformed shape for both flight and ground tests. The Global 7500 has a wing span of 31.7 m [33]. A sketch of the DADTT test rig is presented in Fig. 1.

This study, led in the Bombardier Aviation's Experimental department facility during certification tests, presents the results of deflection and twist angle calculations led on the Global 7500 complete representative structure's left wing DADTT test article. Analytical methods and NN are used for this purpose and their results are discussed. This paper is organized as follows: the Ko theory and Meng's model are detailed in Section 2. Section 3 presents the experimental setup, the tests and the data acquisition and processing. The Ko theory and the Meng's model are compared in Section 4. The deflection and twist angle calculations using the analytical model chosen in Section 4 and using NN are presented and discussed in Section 5. Finally, Section 6 concludes this work.

2. Background

This section aims at presenting both the Ko theory and Meng's model.

2.1. Ko theory

Supposing that a FBG with n distributed strain measurement points is bonded along the span of a wing and that x_i denotes the 1D coordinate of the i^{th} strain measurement point ($i = 1,2,3 \ldots,n$) along the FBG, the distance between the $(i-1)^{th}$ and the i^{th} ($i \geq 2$) strain measurement points is defined as

$$\Delta l_i = x_i - x_{i-1}. \tag{2}$$

The model requires the distance to the neutral axis, C, as an input parameter. It represents the distance between the FBG and the axis of the structure for which the resulting bending strain is equal to zero. In complex geometry wings, the position of the neutral axis is not accurately known. Indeed, its position can change depending on the applied loads. In linear mechanics, the strain resulting from bending evolves linearly from the surface to the neutral axis. Thus, if two FBGs are installed on the wing and symmetrically opposed, one on the upper skin and the other one on the lower skin, the distance between the FBGs and the neutral axis can then be expressed as [2]

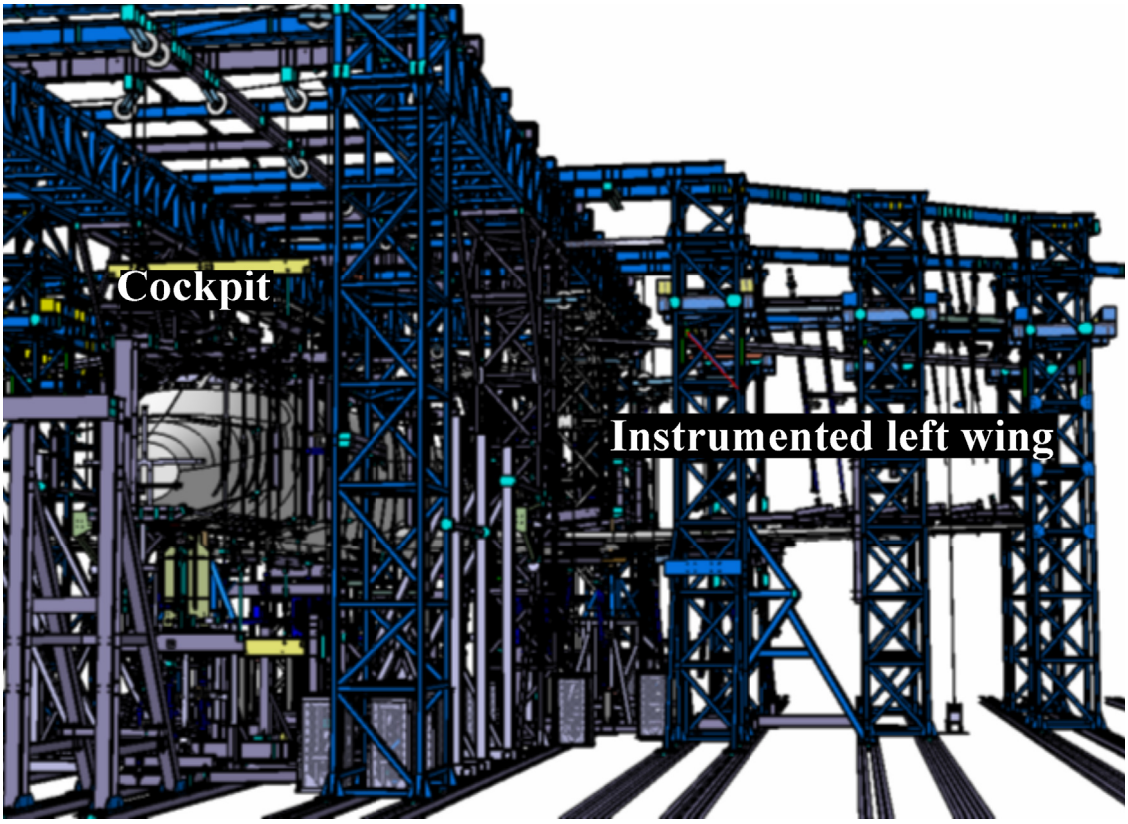

Fig. 1. Durability and damage tolerance test rig of the Global 7500 complete representative structure.

$$C_{top,i} = \frac{\varepsilon_{top,i}}{\varepsilon_{bottom,i} - \varepsilon_{top,i}} h_i \tag{3}$$

and

$$C_{bottom,i} = \frac{\varepsilon_{bottom,i}}{\varepsilon_{bottom,i} - \varepsilon_{top,i}} h_i \tag{4}$$

where h represents the distance between the FBGs located on the upper and lower skins (wing thickness). The subscripts *top* and *bottom* refers to the FBGs installed on the upper and lower skins, respectively.

The deflection is computed as [2]

$$y_i = \frac{\Delta l_i^2}{6C_{i-1}} \left[\left(3 - \frac{C_i}{C_{i-1}} \right) \varepsilon_{i-1} + \varepsilon_i \right] + y_{i-1} + \Delta l_i \tan(\theta_{i-1}) \tag{5}$$

in which the spanwise angle (slope) θ is defined as

$$\tan(\theta_i) = \frac{\Delta l_i}{2C_{i-1}} \left[\left(2 - \frac{C_i}{C_{i-1}} \right) \varepsilon_{i-1} + \varepsilon_i \right] + y_{i-1} + \tan(\theta_{i-1}). \tag{6}$$

Note that, in Equations (5) and (6), i is superior or equal to 2. It implies that the deflection and the spanwise angle at the first measurement point (y_1 and θ_1) must be defined as boundary conditions.

If $y_{leadingedge,i}$ and $y_{trailingedge,i}$ represent the calculated deflections close

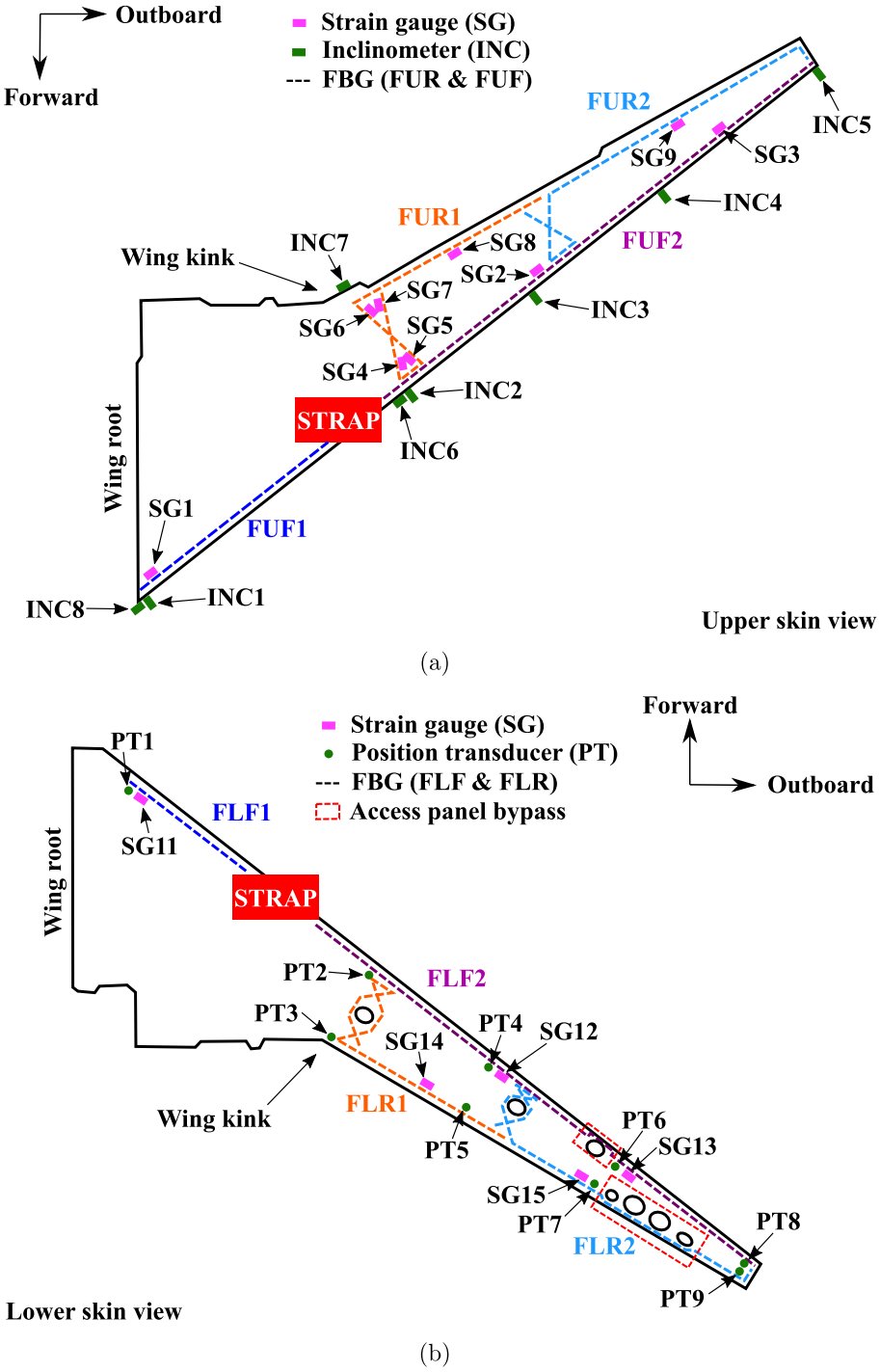

Fig. 2. Sensor locations on the left wing panels.

to the leading and trailing edges, respectively, the twist angle φ_i can be expressed as [2]

$$\varphi_i = \sin^{-1}\left(\frac{y_{leadingedge,i} - y_{trailingedge,i}}{d_i}\right) \tag{7}$$

where d_i represents the distance between the FBGs located at the leading and trailing edges, at the i^{th} measuring point.

2.2. Meng's model

Meng's model is a continuous model. If x denotes the 1D coordinate along the FBG, the curvature is expressed as [19]

$$\kappa(x) = \frac{\varepsilon(x)}{C(x)} \tag{8}$$

where C is computed using Equations (3) and (4). The spanwise angle is then expressed as

$$\theta(x) = \int_0^x \kappa(x)\mathrm{d}x + \theta(0) \tag{9}$$

where $\theta(0)$ is a boundary condition representing the spanwise angle at the first measuring point. Finally, the deflection can be computed as

$$y(x) = \int_0^x \cos(\theta(x))dx + y(0) \tag{10}$$

in which $y(0)$ is the deflection as the first measuring point and is a boundary condition. The twist angle can be computed using Equation (7).

3. Experimental setup, tests and data acquisition

3.1. Experimental setup

3.1.1. Fiber Bragg gratings

The Global 7500 wing skin panels are made in chromic acid anodized and shot peened aluminum alloys. The surfaces on which the FBG were installed were manually sanded with 320 grit sand paper and then cleaned with a degreaser and with isopropyl alcohol. The FBGS AGF-A3A4-000 FBGs were bonded using Micro-Measurements M-BOND 200 adhesive. A protective layer of Momentive RTV108 silicone was applied on the FBGs.

Eight FBGs were installed on the left wing: two FBGs along the front spar and two FBGs along the rear spar, on the lower and upper skins. A schematics of the FBGs location on the wing panels is presented in Fig. 2. The FBGs installed along the rear spar also form cross patterns between the front and rear spars. The absence of FBGs along the rear spar between the wing root and the wing kink, on the upper and lower skins, can be noted. This zone was too difficult to access on the test rig. The presence of two loading straps at the front spar, represented by red rectangles in Fig. 2 (a) and (b), prevented the installation of FBG in these areas. On the lower skin, access panels had to be bypassed. The strain measurements obtained in these bypass zones, represented by red doted rectangles in Fig. 2(b), were not used to calculate the deflection since the FBGs located on the upper and lower skins were not superimposed and Equations (3) and (4) could not be used. The names, locations and lengths of the FBGs are given in Table 1. The FBGs nomenclature is defined as follows: the first letter (F) stands for Fiber, the second letter, U or L, stands for Upper skin or Lower skin and the last letter, F or R, stands for Front spar or Rear spar.

The FBGs could not be installed directly on the spars due to the presence of loading pads used to apply the loads on the wing. The FBGs were installed at 10 cm away from the spars, aft of the front spar and forward of the rear spar, to avoid eventual strain concentration resulting from the forces applied by the loading pads. As an example, the position of the FBG FUF2 with respect to the front spar is presented in Fig. 3.

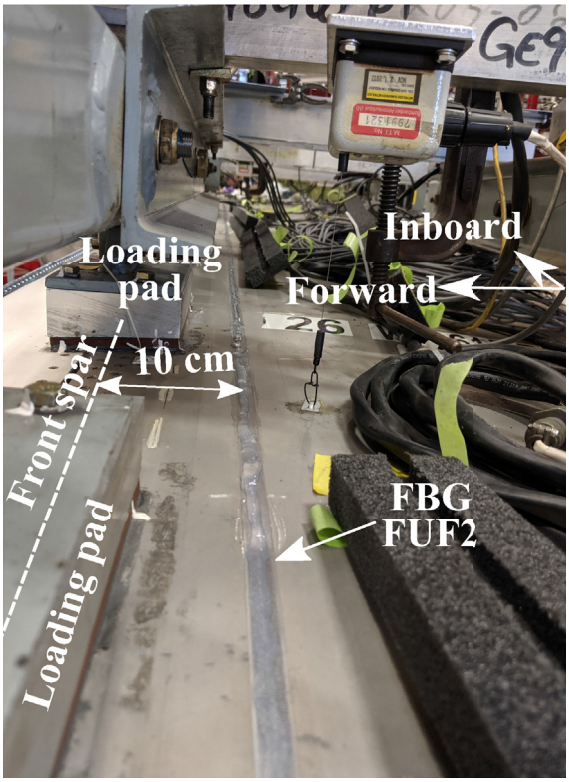

Fig. 3. Position of the FBG FUF2 with respect to the front spar.

Table 1
List of the installed FBGs with their lengths and locations.

	Length (m)	Location/remark
FUF1	5.6	Upper skin, front spar, from wing root to loading strap
FUF2	10.0	Upper skin, front spar, from loading strap to wing tip
FUR1	8.7	Upper skin, rear spar, from wing kink to mid-wing
Cross pattern		
FUR2	9.3	Upper skin, rear spar, from mid-wing to wing tip
Cross pattern and chordwise at wing tip		
FLF1	5.8	Front spar, lower skin, from wing root to loading strap
FLF2	10.7	Front spar, lower skin, from loading strap to wing tip
Access panels bypass		
FLR1	9.0	Lower skin, rear spar, from wing kink to mid-wing
Cross pattern		
FLR2	9.9	Lower skin, rear spar, from mid-wing to wing tip
Cross pattern, access panel bypass and chordwise at wing tip		

3.1.2. Strain gauges

Fourteen Micro-Measurements CEA-13-125UN-350 unidirectional strain gauges were installed along the FBGs to be used as strain measurement references in order to verify the validity of the FBGs strain measurements. The strain gauges were installed to measure the strain in a direction parallel to the FBGs at a distance between 3 and 10 mm from the latter. The strain gauges locations are presented in Fig. 2 and

Table 2
Strain gages locations and corresponding FBGs.

	FBG	Location
SG1	FUF1	Wing root, upper skin
SG2	FUF2	Near mid-wing, upper skin
SG3	FUF2	Near 3/4 wing, upper skin
SG4	FUR1	Cross pattern, upper skin
SG5	FUR1	Cross pattern, upper skin
SG6	FUR1	Cross pattern, upper skin
SG7	FUR1	Cross pattern, upper skin
SG8	FUR1	Near mid-wing, upper skin
SG9	FUR2	Near 3/4 wing, upper skin
SG11	FLF1	Wing root, lower skin
SG12	FLF2	Near mid-wing, lower skin
SG13	FLF2	Near 3/4 wing, lower skin
SG14	FLR1	Near mid-wing, lower skin
SG15	FLR2	Near 3/4 wing, lower skin

described in Table 2.

3.1.3. Position transducers

Nine cable extension position transducers Celesco PT101 were installed to measure the wing deflection. The cables were attached to the lower skin while the sensors were fixed on the hangar ground, 4.5 m below the wing. Their locations are presented in Fig. 2(b) and described in Table 3.

3.1.4. Inclinometers

Eight inclinometers Turk B1N360V-Q20L60-2LU3-H1151 were installed on the wing to measure the spanwise and twist angles. Their locations are indicated in Fig. 2(a) and listed in Table 4. The inclinometers were installed on the spars. Inclinometers INC1 to 5 were used to measure the wing twist while the inclinometers INC6 to 8 measured the spanwise angle and were used as input for the analytical model boundary conditions.

3.2. Tests

3.2.1. Fatigue tests

The first tests performed on the DADTT were fatigue tests. These tests consisted in simulating flight load conditions for an equivalent of three times the design service goal. Ten different types of short, medium and long mission flights, from towing to engines shut down, were repeated.

Table 3
Position transducer locations.

	Location
PT1	Front spar, wing root
PT2	Front spar at wing kink
PT3	Rear spar, wing kink
PT4	Front spar near mid-wing
PT5	Rear spar, near mid-wing
PT6	Front spar near 3/4 wing
PT7	Rear spar, near 3/4 wing
PT8	Front spar near wing tip
PT9	Rear spar, near wing tip

Table 4
Inclinometers locations.

	Location	Measured angle
INC1	Front spar, wing root	Twist
INC2	Front spar, wing kink	Twist
INC3	Front spar, near mid-wing	Twist
INC4	Front spar, near 3/4 wing	Twist
INC5	Front spar, wing tip	Twist
INC6	Front spar, wing kink	Spanwise
INC7	Rear spar, wing kink	Spanwise
INC8	Front spar, wing root	Spanwise

This fatigue test campaign aimed at demonstrating, according to the Federal Aviation Administration (FAA), Transport Canada (TC) and the European Union Aviation Safety Agency (EASA) standards, that the Global 7500 can withstand three fatigue lives, without showing any critical failure resulting from natural crack initiation or accidental damage.

A simulated flight composed of a subset of load cases applied on the test article, in the last quarter of the third fatigue life, was used to obtain the results presented in this paper. It corresponds to a flight suffering significant wing deflections.

Just before the simulated flight, the Global 7500 representative structure was put in a 0 g position (own weight sustained) to record the zero strain state reference (λ_{ref} in Equation (1)). The wing deflection and twist were also considered to be null at the 0 g position.

The FBGs located along the rear spar and the spanwise inclinometers were not installed at the time the fatigue tests were performed. Thus, only the front spar deflection was calculated.

3.2.2. Residual strength tests

The Residual Strength Tests (RSTs) were performed once the fatigue tests campaign was completed. During these tests, critical static load cases were applied. The objective is to demonstrate that the damages that appeared during the fatigue tests and cracks voluntarily induced would not result in a critical failure, according to FAA, TC and EASA standards. The data were acquired during four RSTs, chosen for their large bending and/or large wing twist. The four monitored RSTs are listed in Table 5.

Before each RST, the Global 7500 representative structure was put in a 0 g position to record the zero strain state, deflection and twist references. All the sensors mentioned in Section 3.1 were installed during the RSTs campaign. The critical static load cases were applied and released in 10% increments. A picture of the left wing deflection during a RST is presented in Fig. 4. The 0 g position of the wing is also indicated.

3.3. Data acquisition and processing

A Sensuron RTS125+ optical frequency domain reflectometry system was used to acquire the FBGs data. The results from the eight FBGs were acquired simultaneously at rates of 11 Hz and 9 Hz during the fatigue test and RSTs, respectively. The spacing between each strain measuring point along the FBGs was 6.35 mm. During the RSTs, data were acquired during 5 s for each steady loading level and then averaged over the time period.

The position transducers, strain gauges and inclinometers measures were recorded using Bombardier Aviation's data acquisition system. They were set to zero each time the Global 7500 was put in the 0 g position. One measurement was recorded for each different load case applied during the fatigue test and for each increment during the RSTs.

Sensuron machine and Bombardier Aviation's data acquisition system timestamps were synchronized using the signal received on the Bombardier Aviation Global Positioning System antenna.

All data were processed using the programming language `Python`, with `NumPy` and `Pandas` libraries. Equations (9) and (10) integrals were computed using the composite trapezoidal rule with the `NumPy` function `trapz`. Equations (3) and (4) required perfectly symmetrical opposed strain $\varepsilon_{top,i}$ and $\varepsilon_{bottom,i}$. For this purpose, $\varepsilon_{bottom,i}$ were interpolated using the linear interpolation `NumPy` function `interp` to match the spanwise locations of the $\varepsilon_{top,i}$ data. This function was also used to interpolate the

Table 5
Monitored residual strength tests.

	Description
RST1	Rudder Maneuver
RST2	Positive Balance Maneuver
RST3	Tail Down Dynamic Landing
RST4	Positive Balance Maneuver

missing data at the access panel bypasses and at the loading straps.

All the deflections, strain and angles are normalized with respect to their respective maximum measured values for confidentiality reasons.

4. Model selection

The deflection of a beam was simulated with a FEM to compare the Ko theory and Meng's model. Both models were deliberately not compared with the experimental results obtained on the DADTT. Indeed, the errors induced by the lack of data at the access panel bypasses and the loading straps, the other than pure bending induced measured strain (not parallel to the FBGs), the apparition of local strain concentrations at the wing's ribs, etc … were impossible to quantify and could have discredited the comparison.

4.1. Finite element model validation

A FEM beam with a 1.81 m length (L) and a 76.2 by 9.5 mm rectangular cross section was solved with NASTRAN. The beam dimensions were arbitrarily chosen. The material properties are a Young modulus (E) of 68 GPa and a Poisson's ratio of 0.33, representative of typical aluminum alloys used in the aerospace industry. The beam was composed of seven nodes, equally spaced and linked with CBAR beam elements. All translations and rotations at one end of the beam were set to zero and a vertical displacement was applied on the other end to simulate a deflection. The applied displacements, D, were 50, 100, 200, 300, 400, 500 and 600 mm. The displacements were imposed perpendicularly to the smallest cross section area moment of inertia ($I_Z = 5487.4\ \text{mm}^4$). The strain was obtained, for each node, at the upper mid-with of the cross section. A schematic of the FEM is presented in Fig. 5.

The strains obtained with the FEM (ε_{FEM}) along the beam span, X, were cross-checked with the beam theory and Hooke's law using the commonly known expression

$$\varepsilon_{theory}(X) = \frac{M_Z(X)C}{EI_Z} \tag{11}$$

where C represents the half thickness of the beam and the bending moment M_Z is expressed as

$$M_Z(X) = \frac{3EI_Z D}{L^3}(L - X) \tag{12}$$

The comparisons between the strain distributions obtained with the FEM and those calculated with Equation (11), for all the imposed displacements D, are presented in Fig. 6. The strain unit used in Fig. 6 is the micro-strain ($\mu\varepsilon$), which corresponds to 10^{-6} mm/mm. It should be noted that the strain distributions obtained with the FEM are in perfect agreement with the ones calculated according to the beam theory. This result was expected since the CBAR elements are derived from the beam theory.

The obtained strain distributions were then approximated with a first order polynomial function expressed as

$$\varepsilon_{FEM,approx}(X) = aX + b. \tag{13}$$

Parameters a and b values are given in Table 6.

4.2. Ko theory and Meng's model comparison

The Ko theory and Meng's model were then used to calculate the deflections using a strain measurement distribution of 6.35 mm, corresponding to the strain measurement distribution that will be measured with the Sensuron system. The deflections were also calculated using a 250 mm strain measurement distribution to verify both model's behavior with a lack of data. This situation could correspond to the access panel

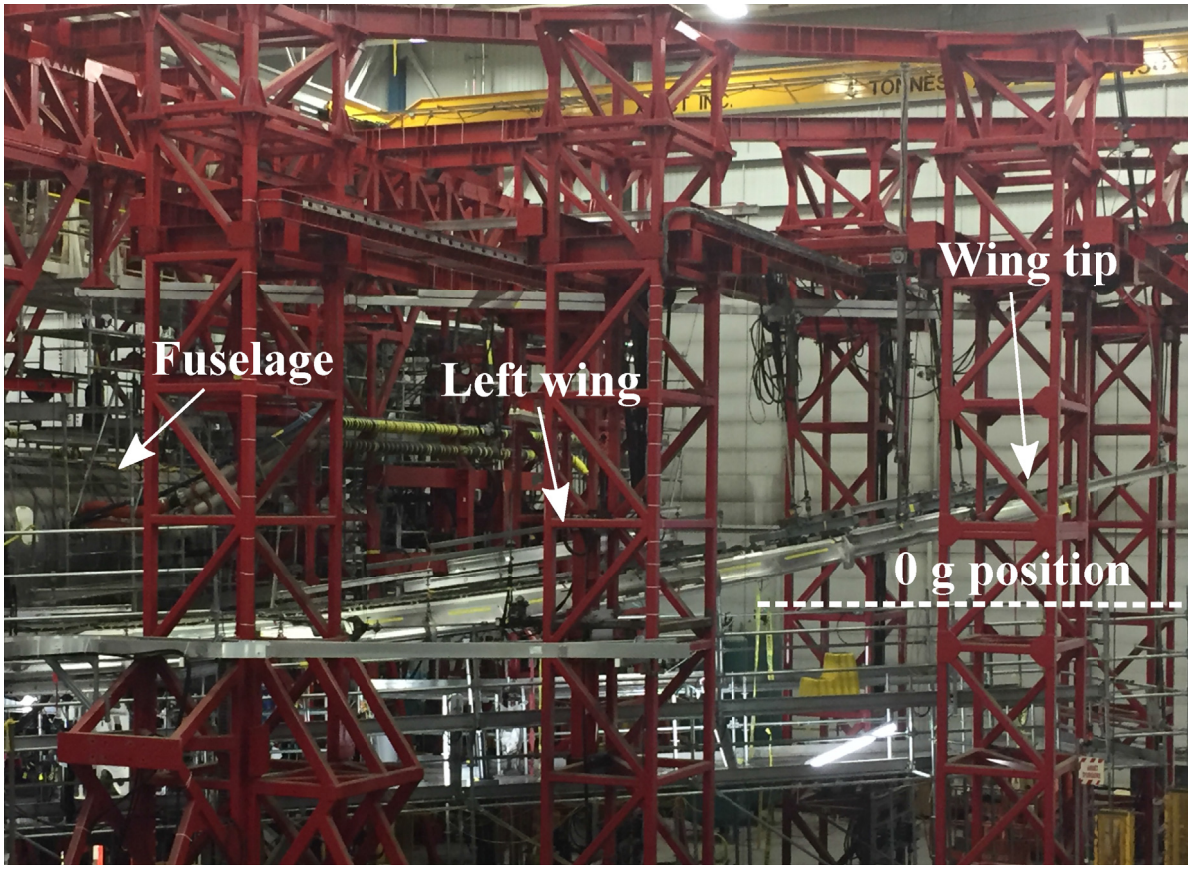

Fig. 4. Global 7500 left wing deflection during a RST. The position of the wing at the 0 g position is indicated.

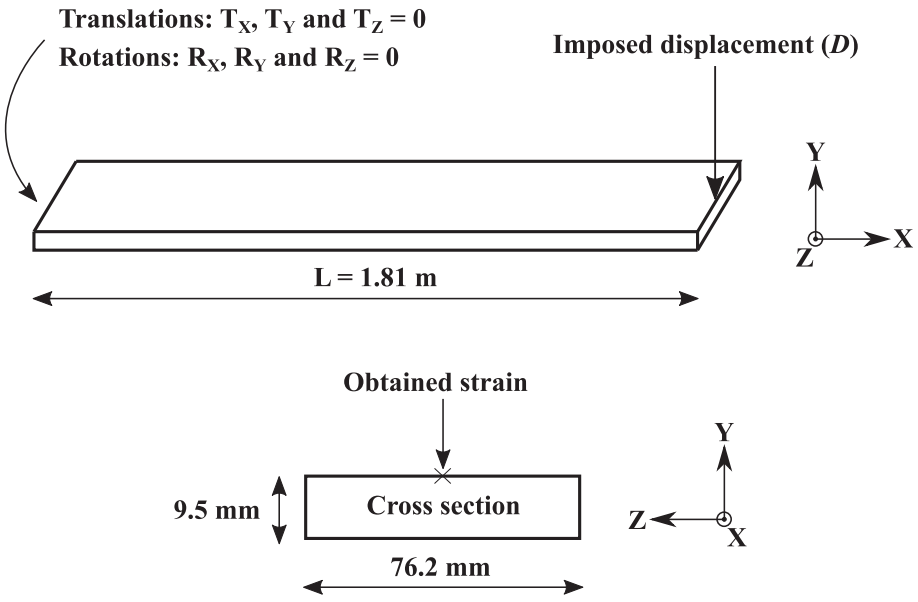

Fig. 5. Schematic of the finite element model.

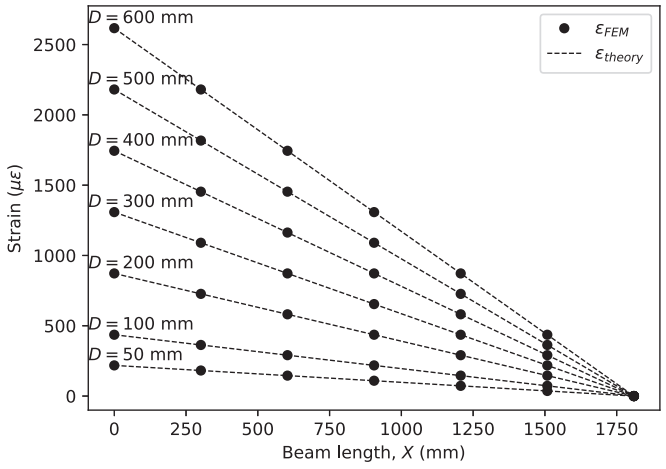

Fig. 6. Comparison between the strain distributions obtained with the finite element model (ε_{FEM}) and those calculated using the beam theory (ε_{theory}).

Table 6
Parameters a and b from Equation (13).

D (mm)	a ($\mu\varepsilon$/mm)	b ($\mu\varepsilon$)
50	−0.12	218.06
100	−0.24	436.11
200	−0.48	872.23
300	−0.72	1308.34
400	−0.96	1744.45
500	−1.20	2180.57
600	−1.45	2616.68

bypasses and the loading straps regions on the wing. The calculated deflections were compared to the deflections obtained with the FEM. Validation was done using the deflection calculated with the beam theory, y_{theory}, expressed as

$$y_{theory}(X) = -\frac{PX^2}{6EI_z}(3L - X) \tag{14}$$

where P represents the load that should be applied to obtained the corresponding deflection and is expressed as

$$P = -\frac{3EI_zD}{L^3}. \tag{15}$$

The deflections calculated using the Ko theory and Meng's model with strain measurement distributions of 6.35 mm and 250 mm are presented in Fig. 7 (a) and (b), respectively. The deflections obtained with the FEM and calculated with the beam theory are also represented. It can be observed that the two latter are in perfect agreement. The Ko theory and Meng's model deflection percentage errors are presented in Fig. 8 and were calculated as

$$y_{FEMerror}(X) = \left(\frac{y_{pred}(X)}{y_{FEM}(X)} - 1\right)100 \tag{16}$$

where y_{FEM} represents the deflection obtained with the FEM and y_{pred} represents the deflection calculated either with the Ko theory or Meng's model. The deflection errors at $X = 0$ mm were not represented on Fig. 8 since the deflection at this location is a boundary condition for both models.

For a strain measurement distribution of 6.35 mm, Figs. 7(a) and 8 show that the error obtained with the Ko theory is lower than one obtained with Meng's model. For an applied deflection $D = 600$ mm, the Ko theory percentage error is −0.09% at the beam tip while it is −2.64% for Meng's model. Both models underpredict the beam deflection but give a good representation of the beam deformed shape.

On the other hand, for a strain measurement distribution of 250 mm, the Ko theory results are less accurate than the ones obtained with Meng's model. At the beam tip, for an applied displacement $D = 600$ mm, the error obtained with the Ko theory is −3.91% while it is −3.11% for Meng's model. Also, Fig. 7 (b) shows that, for $D \geq 200$ mm, the deformed shape of the beam is not well predicted by the Ko theory. For example, at the FEM grid located at $X = 905$ mm, the Ko theory percentage error is −7.90% while it is −0.80% for Meng's model.

It can be concluded that the Ko theory predictions are more accurate than the ones of Meng's model for a 6.35 mm strain measurement distribution. However, the Ko theory becomes unstable if the strain measurements distribution is increased and the deformed shape is no more well predicted. Meng's model is less sensitive to the strain measurement distribution and should thus result in more reliable predictions in the case of the Global 7500 wing for which loading straps and access panel bypasses are regions where strain data are missing. Meng's model will

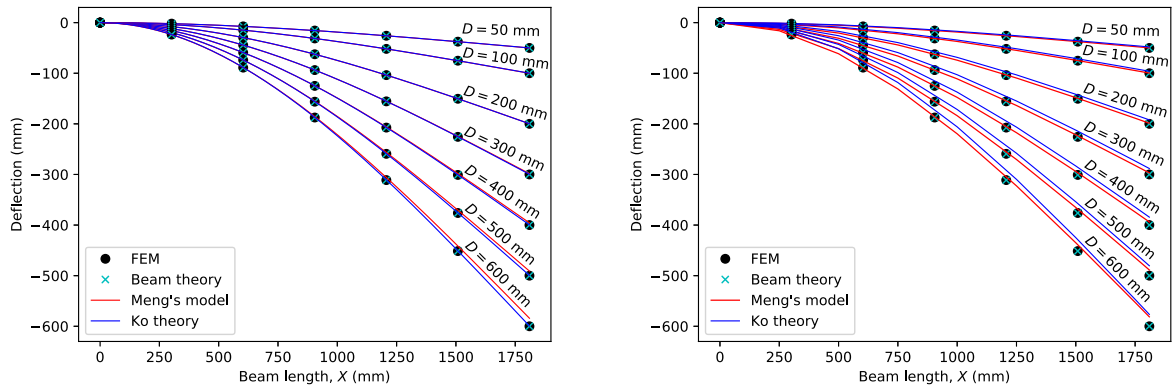

Fig. 7. Ko theory and Meng's model deflection results using strain measurement distributions of (a) 6.35 mm and (b) 250 mm compared to those obtained with the finite element model (FEM) and calculated using the beam theory.

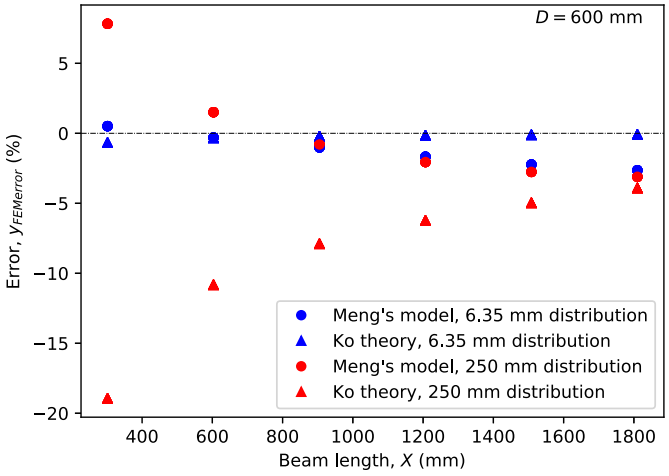

Fig. 8. Ko theory and Meng's model calculated deflection errors for strain measurement distributions of 6.35 mm and 250 mm and for an applied deflection, D, of 600 mm.

thus be used thereafter.

5. Results and discussion

5.1. Comparison with strain gauges

Strain gauges are commonly used in the aerospace industry as reference for strain measurements. The strain measurements obtained with the strain gauges and the FBGs are compared. The relative error (in percentage) of the FBGs strain measurements, when compared to the strain gauges ones, were calculated for the RSTs, at 100% applied load, as

$$\varepsilon_{error} = \left(\frac{\varepsilon_{FBG}}{\varepsilon_{SG}} - 1\right) 100 \tag{17}$$

where ε_{FBG} and ε_{SG} represent the strain measured by the FBGs and the strain gauges, respectively. The relative errors are presented in Fig. 9. The strain were normalized using the equation

$$\varepsilon_{norm} = \frac{\varepsilon_{SG}}{\varepsilon_{SG,max}} \tag{18}$$

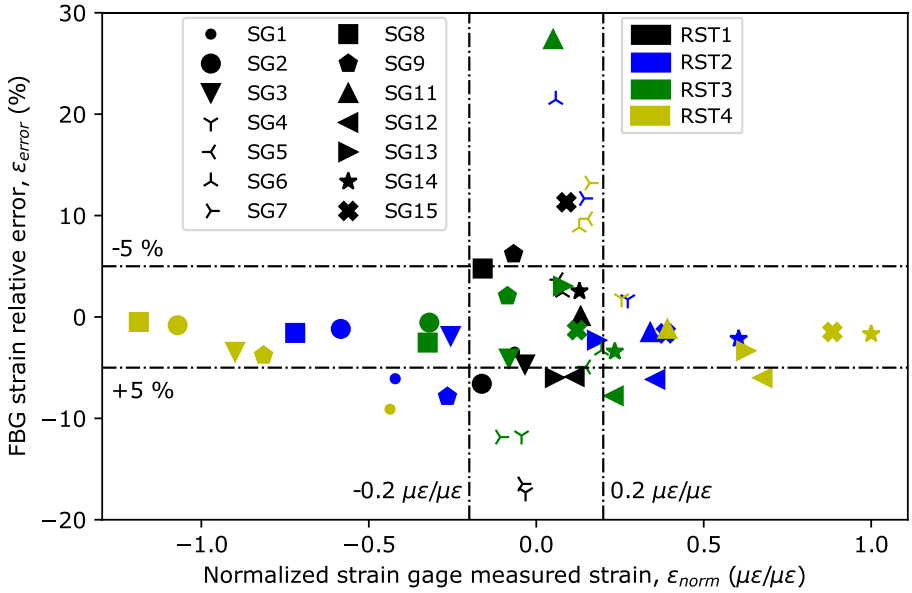

Fig. 9. FBGs strain measurements relative errors, ε_{error}, for each monitored RST at 100% load applied. Each marker represents a strain gauge and each color represents a RST. ±5% relative error and ±0.2 $\mu\varepsilon/\mu\varepsilon$ normalized strain lines are also plotted.

where $\varepsilon_{SG,max}$ represents the maximum strain measured with strain gauges. $\varepsilon_{SG,max}$ has a value between 2000 and 3000 $\mu\varepsilon$.

Two strain measurements are not plotted in Fig. 9 due to their large relative errors: SG1 for RST3 (-0.02 $\mu\varepsilon/\mu\varepsilon$; -256%) and SG5 for RST2 (0.02 $\mu\varepsilon/\mu\varepsilon$; 128%). These large relative strain errors are due to the small strain measured. Two ± 0.2 $\mu\varepsilon/\mu\varepsilon$ vertical dotted lines were plotted on Fig. 9. 0.2 $\mu\varepsilon/\mu\varepsilon$ corresponds to a measured strain between 400 and 600 $\mu\varepsilon$ (0.0004 and 0.0006 mm/mm) below which the strain is considered as not significant.

Two horizontal dotted lines at $\pm 5\%$ were also plotted in Fig. 9. The relative error is considered acceptable inside these two boundaries.

Six strain measurements are outside of the $\pm 5\%$ relative error boundaries for significant measured strain, namely SG1 for RST2 and RST4, SG9 for RST2 and SG12 for RST2, RST3 and RST4. They are evenly distributed between tension and compression, eliminating the existence of a tendency for the FBGs to be less accurate in one of these strain state. These relative errors are likely to be due to high strain gradients, since torque was also applied to the wing and the distances between the FBGs and the strain gauges could be as large as 10 mm due to experimental constraints. The fact that the FBG relative strain measurement error, at the location of SG1, is smaller for RST2 than RST4 whilst the measured strain is in the same order of magnitude (-0.4 μm), for both RSTs, tends to reinforce this hypothesis.

Fig. 9 shows that the large majority of FBGs relative errors for measured strain higher than 0.2 $\mu\varepsilon/\mu\varepsilon$, in terms of absolute value, are within the ± 5 % boundaries. The strain measured by the strain gauges and the FGBs are thus considered to be in good agreement.

5.2. Deflection analytical calculations

5.2.1. Fatigue test

Throughout the load cases applied during the analysed flight, front spar deflections were calculated using Meng's model. The deflection measurements derived from the position transducer PT1 were used as a boundary condition for the model. The inclinometer INC8 was not installed at the time of the fatigue test and thus the spanwise angle at the wing root was set to 0°.

The comparison between calculated and measured deflections, depending on the flight duration, are presented in Fig. 10. For clarity, Fig. 10 was divided into two subfigures: Fig. 10(a) presents the deflections at the locations of PT2 and PT6 while Fig. 10(b) presents those at the locations of PT4 and PT8. Take-off and landing are also indicated in Fig. 10. The left wing span, from wing root to wing tip was normalized using the equation

$$WS_{norm} = \frac{WS_{pos}}{WS_{max}} \tag{19}$$

where WS_{pos} is the position on the wing and WS_{max} is the left wing span. The deflections were also normalized using the equation

$$y_{norm} = \frac{y}{y_{max}} \tag{20}$$

where y represents the measured or calculated deflection and y_{max} is the largest overall measured deflection (between 1 and 2 m during RST4).

The two taxiing simulations (before take-off and after landing) are clearly visible on Fig. 10: the wing is submitted to down-bending oscillations due to its own weight and the on-ground movement of the aircraft. Enlargements of these regions are enclosed to enhance the reading. The in-flight simulation is also observable due to the up-bending position of the wing which registers normalized deflections up to 0.6 m/m. The calculated and measured deflections seem to be in good agreement during the in-fight simulation at the locations of the four position transducers, which suggest that the deformed shape of the wing is well predicted by the model. However, discrepancies are observable during the taxiing simulations. This could be explained by the fact that the wing deflection amplitudes are small during the taxiing (between 0 and -0.09 m/m) and thus the errors attributable to other than vertical bending induced strain such as twist or horizontal bending strain are more pronounced.

The measured and calculated deflections depending on the normalized wing span for the loading cases leading to the maximum and minimum deflections are presented in Fig. 11. The deformed shape of the wing is well predicted by the model for both load cases.

The calculated deflection relative errors (in percentage) when compared to the measured ones were calculated as

$$y_{error} = \left(\frac{y_{Pred}}{y_{PT}} - 1\right) 100 \tag{21}$$

where y_{PT} is the measured deflection and y_{Pred} is the corresponding predicted deflection. The relative errors depending on the normalized measured deflection are presented in Fig. 12. An enlargement of the results is enclosed in Fig. 12 to enhance the reading of the large deflections results.

The relative errors are larger than 10% for small deflections and are between -1 and 4% for normalized deflections higher than 0.2 m/m (between 0.2 and 0.4 m). As mentioned before, the large relative errors for the small deflections might be due to parasite strain measurements such as those induced by horizontal bending and twist. Moreover, the errors due to strain approximation at the loading strap and at the access panel bypasses might have a greater detrimental effect on the prediction of smallest deflections. Also, using Equation (21), a small difference in the measured and calculated deflections for a small measured deflection would lead to a large percentage relative error.

When compared to the error obtained using Meng's model in a virtually perfect environment (see Section 4), which were up to 3%, relative errors of -1 to 4% can be considered as good result for calculation led on a real wing submitted to complex load cases and for which the spanwise angle at the first measurement point was unknown and set to 0°. These errors are in the same order of magnitude of the 2.4% relative error obtained by Jutte et al. [2] on a wing submitted to vertical bending only.

It can be concluded that FBGs installed along the Global 7500 wing front spar allow to calculate its deflection with an acceptable accuracy.

5.2.2. Residual strength test

The front spar deflections were calculated, using Meng's model, for each monitored RST at 100% applied load. The deflections were calculated two times; the first time starting at the wing root using the measures derived from PT1 and INC8 as boundary conditions and secondly starting at the wing kink using the measurements derived from PT2 and INC6 as boundary conditions. The deflections starting at the wing kink were calculated to have a fairer comparison with the rear spar deflections which are also calculated from the wing kink. The relative errors, calculated using Equation (21), are presented in Table 7.

The spanwise angle relative errors at the location of INC6, expressed as

$$\Delta\theta = \theta_{Pred} - \theta_{INC6} \tag{22}$$

where θ_{Pred} and θ_{INC6} represent the predicted spanwise angle and the measures derived from INC6, respectively, are also presented in Table 7. Finally, the normalized deflections measured by the position transducer PT8, $y_{norm,PT8}$, obtained using Equation (20), are also presented in Table 7.

The results presented in Table 7 show that, for deflections calculated from the wing root, the smaller the deflection, the larger the relative error on the calculated deflection, which is in accordance with the results obtained during the fatigue test. However, for RST2 and RST3, the relative errors are larger than 4%, even if the wing tip normalized

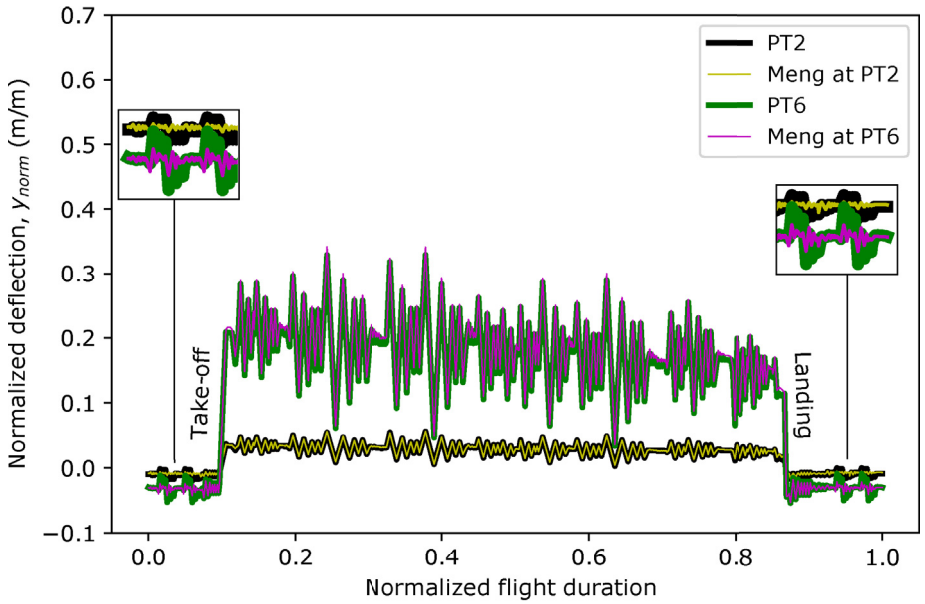

(a)

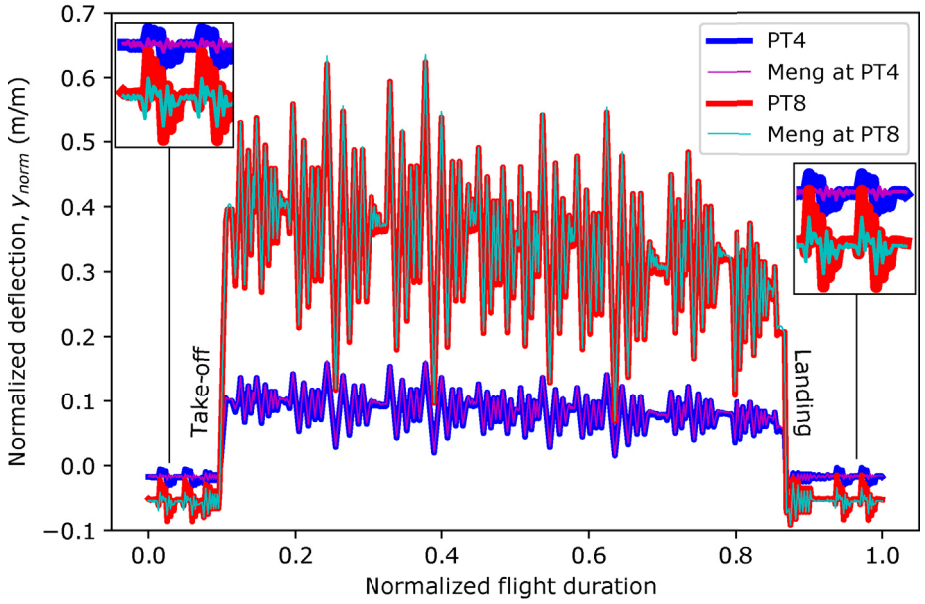

(b)

Fig. 10. Comparison between measured and calculated deflections during the simulated flight at locations of (a) PT2 and PT6 and (b) PT4 and PT8. Enlargements of regions prior take-off and post landing are enclosed.

deflection is larger than 0.2 m/m. It is in contradiction with the fatigue results presented in Fig. 12. However, the wing was submitted to larger torques during the RSTs, which could explain this discrepancy. Despite these large relative errors on the calculated deflections, the calculated wing span angle is in good agreement with the measurements derived from INC6 with a maximal difference of 0.14°.

On the other hand, the front spar deflections calculated from the wing kink show wing tip deflection relative errors inferior or equal to 2%. It suggests that most of the deflection calculation errors are accumulated between the wing root and the wing kink. This suggestion can be put in perspective with the results presented in Fig. 9, in which strain measurement discrepancies larger than 5% were found between the FBG and the strain gauge SG1. It suggests that this region is impacted by high strain gradients. Another explanation could be found in the tapered geometry of the wing inboard of the wing kink. Indeed, Meng's model takes into account the variation of the wing thickness (Equations (3) and (4)) but does not take into account the spar sweep angle.

Due to the smaller relative errors of the front spar deflections calculated from the wing kink, the latter will be used to compare the deflections calculated along the front and rear spars.

The deflection relative errors calculated along the rear spar and the corresponding normalized deflections measured by the position transducer PT9, $y_{norm,PT9}$, are presented in Table 8. Measurements derived from the position transducer PT3 and the inclinometer INC7 were used as boundary conditions for the model. The relative errors, at the wing tip,

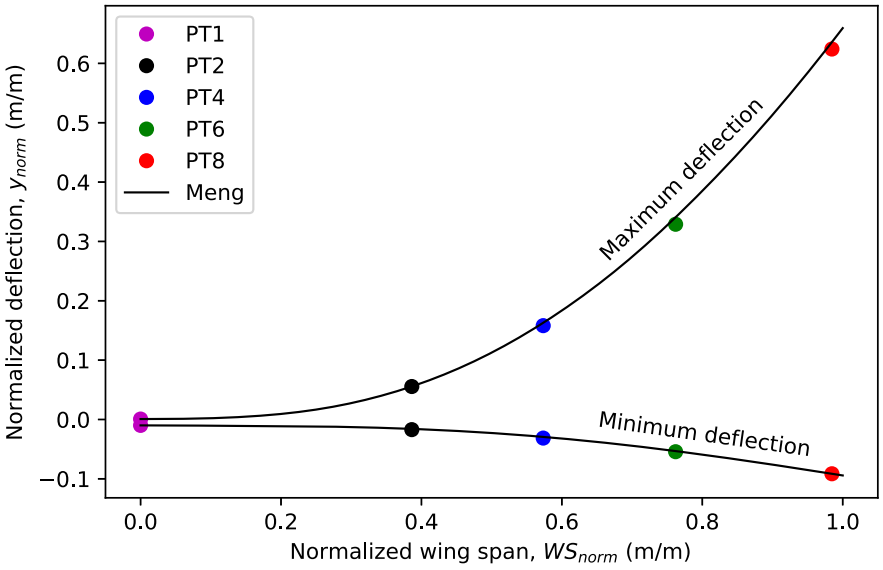

Fig. 11. Calculated and measured minimum and maximum deflections of the simulated flight.

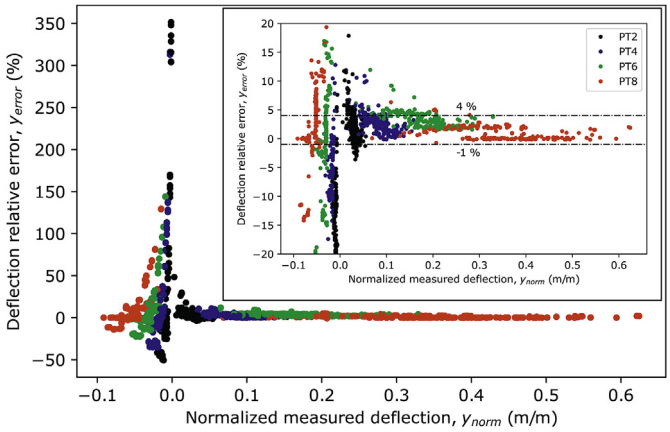

Fig. 12. Simulated flight calculated deflection relative errors depending on the normalized measured deflections.

Table 7
RSTs relative errors (y_{error}) of front spar deflections calculated from the wing root and from wing kink. The differences between the winspan angle calculated and measured by the inclinometer INC6 ($\Delta\theta$) are also presented. The symbol *BC* is used to stipulate that the sensor measurement was used as a boundary condition.

	y_{error} (%)				$\Delta\theta$ (°)	$y_{norm,PT8}$
	PT2	PT4	PT6	PT8	INC6	(m/m)
RST1 from wing root	37.2	20.1	15.7	10.0	0.02	
RST1 from wing kink	*BC*	0.2	2.5	0.3	*BC*	0.13
RST2 from wing root	−0.1	3.9	5.4	4.4	0.14	
RST2 from wing kink	*BC*	1.6	2.9	2.0	*BC*	0.64
RST3 from wing root	79.3	20.1	14.1	7.8	0.05	
RST3 from wing kink	*BC*	1.2	4.0	1.3	*BC*	0.29
RST4 from wing root	−5.8	−0.5	2.1	1.2	−0.01	
RST4 from wing kink	*BC*	0.8	2.3	1.1	*BC*	1.00

are inferior to 1.9% for all monitored RSTs. It suggests that the deflections calculated along the rear spar are in good agreement with the measured deflections.

The calculated and measured normalized deflections at the front and rear spars are compared, for each monitored RST, in Fig. 13. Note that the position transducers PT2 and PT3 were used as boundary conditions and

Table 8
Rear spar calculated deflection relative errors (y_{error}) for the monitored RST.

	y_{error} (%)			$y_{norm,PT9}$
	PT5	PT7	PT9	(m/m)
RST1	13.3	−4.6	−1.9	0.13
RST2	13.9	−1.2	−0.4	0.62
RST3	21.3	0.8	1.8	0.29
RST4	18.8	1.0	1.1	0.97

are thus equal to the calculated deflections. Fig. 13 shows that the relative calculated vertical position of the front spar with regards to the rear spar is, for all the RSTs except RST1 which showed a normalized deflection at the wing tip lower than 0.2, in good agreement. In particular: the front spar deflection is larger than the one of the rear spar for RST2 and RST4 while it is the opposite for RST3. The deformed shaped of the two spars are also well predicted. It is an indication that the twist angle calculation can be performed using Equation (7).

5.3. Twist angles calculation

The twist angles measured during the RSTs, at 100% load applied, are presented in Fig. 14. The twist angles, φ, were normalized as

$$\varphi_{norm} = \frac{\varphi}{\varphi_{\max}} \tag{23}$$

where φ_{max} is the overall maximum twist angle that was measured and has a value between 2 and 5°. A positive angle means that the vertical deflection of the front spar is higher than the one of the rear spar. Fig. 14 shows that the RST2 and 4 present positive twist angles while the twist angles are negative and around 4 to 5 times inferior for RST1 and 3, respectively.

The twist angles of the monitored RSTs were calculated, using Equation (7), with calculated deflections and measurements derived from the position transducers. The results are presented in Fig. 15. The relative twist angle errors were calculated using the following relation:

$$\Delta\varphi = \varphi_{Pred} - \varphi_{INC} \tag{24}$$

where φ_{Pred} represents the predicted twist angle, either using calculated or measured deflections, and φ_{INC} is the measured twist angle. Twist angles were calculated at the locations of INC3, INC4 and INC5. It should

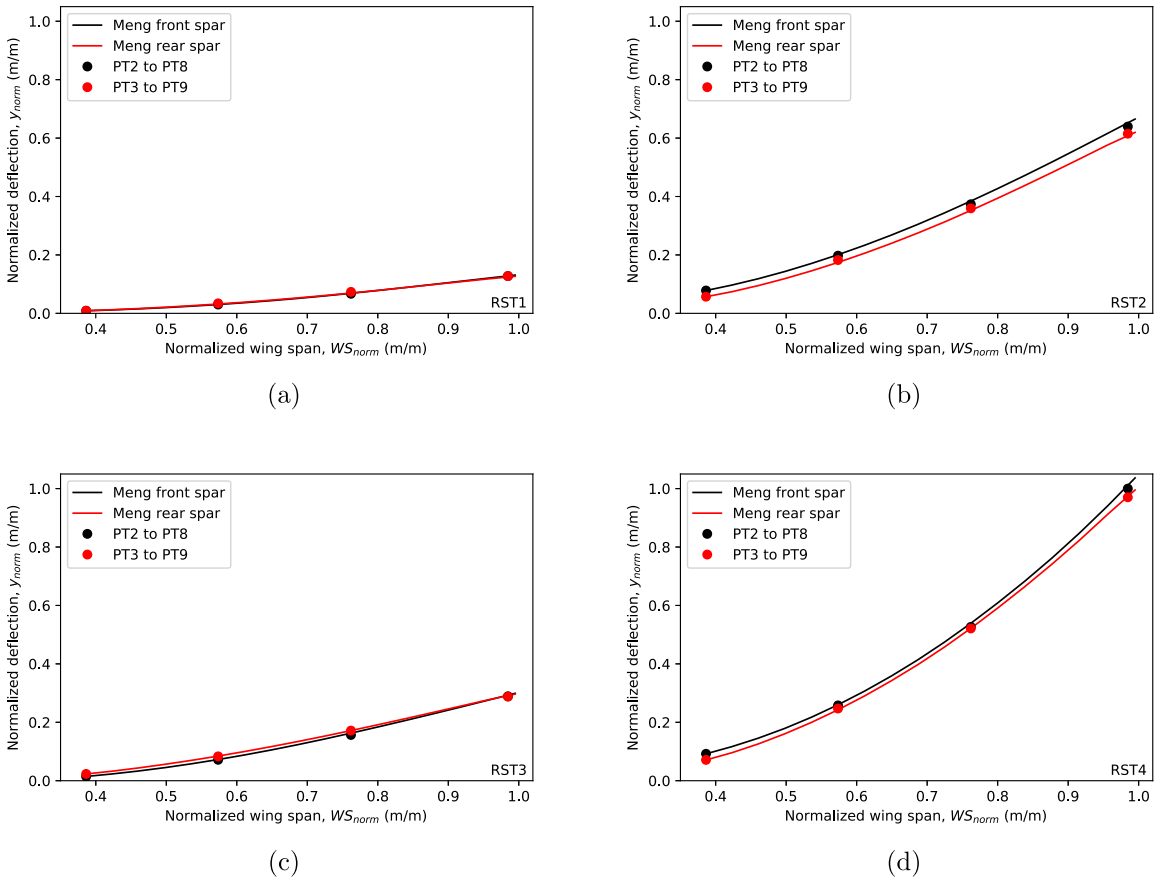

Fig. 13. Comparison of the front and rear spars calculated and measured deflections for (a) RST1, (b) RST2, (c) RST3 and (d) RST4. PT2 and PT3 were used as boundary conditions.

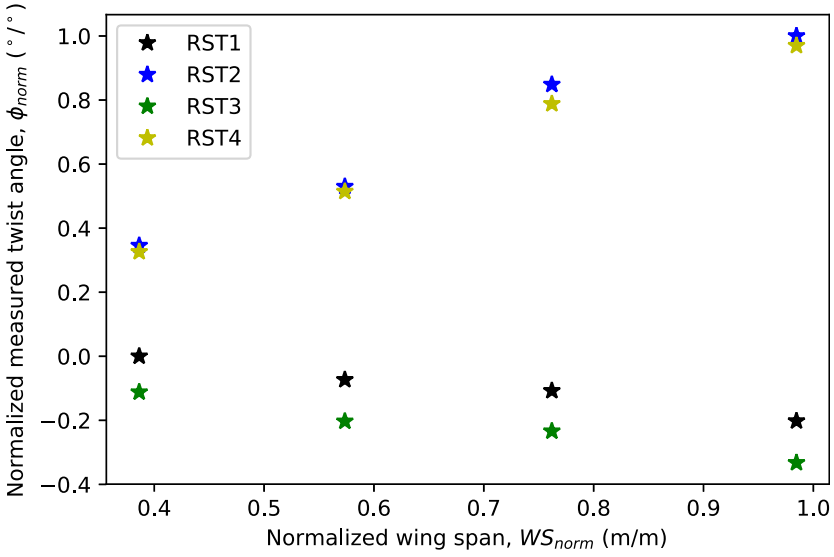

Fig. 14. Inclinometers INC2, 3, 4 and 5 normalized measured twist angles.

be noted that the position transducers PT8 and PT9 are not at the same spanwise location than the inclinometer INC5. However, their positions are assumed to be close enough to the one of INC5 to be compared. The maximum acceptable relative twist angle error targeted was ± 0.5° and two horizontal dotted lines were added on the graphs presented in Fig. 15 to symbolize the targeted error range.

Fig. 15 shows that the twist angle errors increase along the wing span and are, for all the monitored RSTs, out of the targeted range near the wing tip (INC5) for both the calculated and measured deflections. At the location of INC4, all the twist angle errors are out of the targeted range,

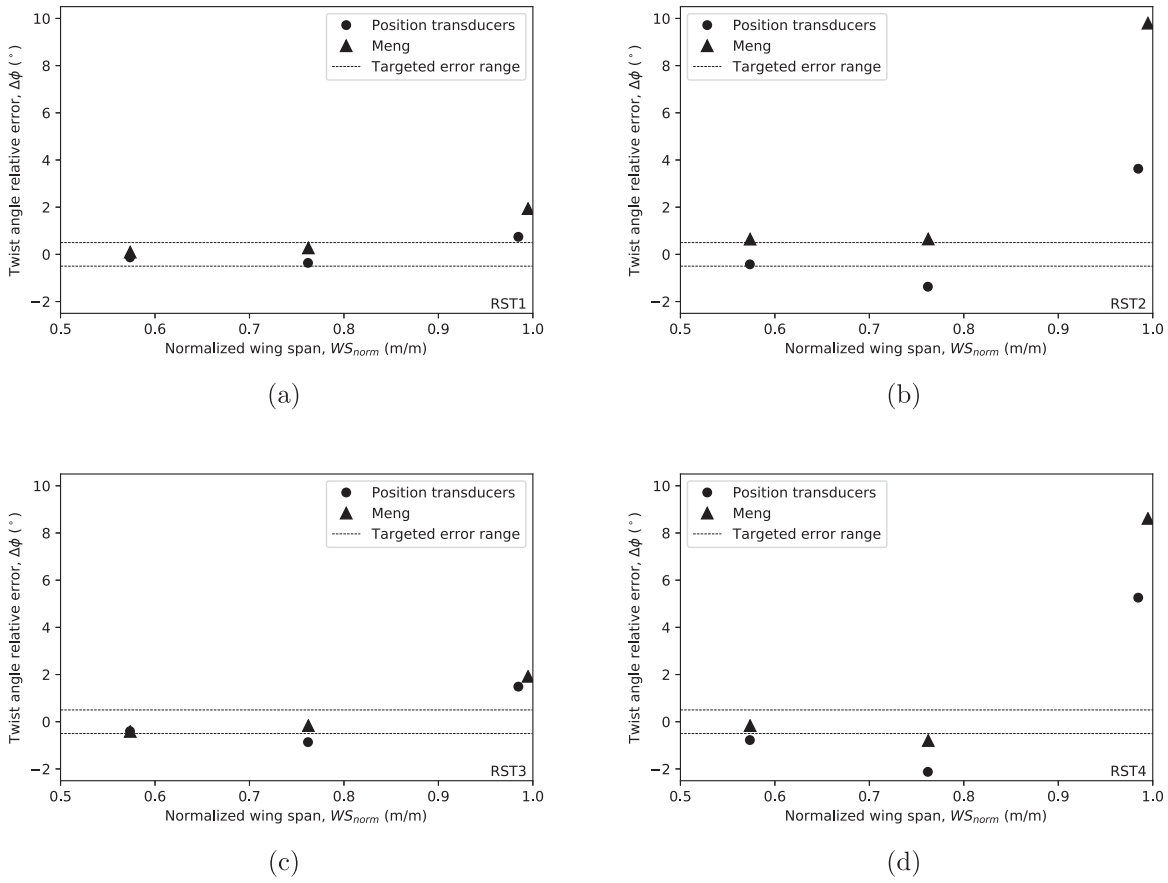

Fig. 15. Twist angles errors, $\Delta\varphi$, calculated using the calculated (Meng) and measured (position transducers) deflections for (a) RST1, (b) RST2, (c) RST3 and (d) RST4. The horizontal dotted lines represent the targeted error range.

except for RST1 and for the calculated deflections of RST3. At the location of INC3, all $\Delta\varphi$ are in the targeted range, except the calculated deflections of RST2 and the measured deflections of RST3.

The calculated twist angles do not satisfy the objective to have a twist angle error in the targeted range, neither calculated using the calculated nor the measured deflections. Similar observations were made by Jutte et al. [2]. Indeed, using Equation (7), small errors in the deflections lead to large errors in the calculated twist angle, especially as the distance between the front and the rear spars decreases. This explains why the error on the twist angle is the largest near the wing tip where the chordwise dimension of the wing is the smallest.

It can be concluded that using calculated or measured deflection difference between front and rear spars is not a suitable method to calculate the twist angle.

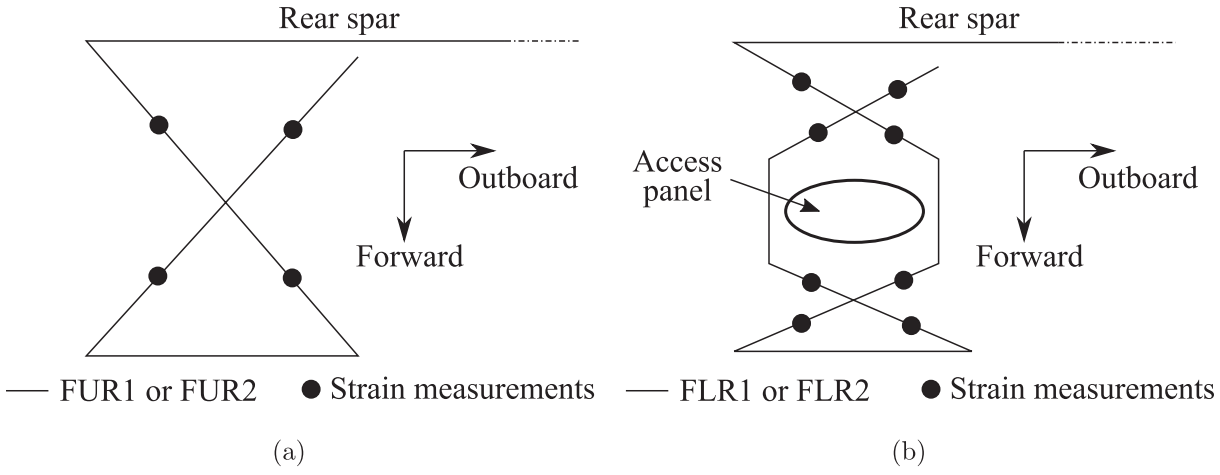

Fig. 16. Schematic of the strain measurement locations on the (a) upper skin and (b) lower skin cross patterns used as input parameters for the neural network.

5.4. Machine learning for deflection and twist prediction

The deflections and twist angles were predicted using a NN. The NN used is a multi-layer perceptron. The function `MLPRegressor` from the `Scikit-learn` library was used for this purpose.

The input parameters are strain measurements from the FBGs. The strain measurements, arbitrarily chosen, are distributed as follows:

- 10 evenly distributed along the front spar on the upper skin, starting at the wing root.
- 9 evenly distributed along the front spar on the lower skin, starting at the wing root.
- 9 evenly distributed along the rear spar on the upper skin.
- 8 evenly distributed along the rear spar on the lower skin.
- 4 on the cross pattern of the FBG FUR1.
- 4 on the cross pattern of the FBG FUR2.
- 8 on the cross patterns of the FBG FLR1.
- 8 on the cross patterns of the FBG FLR2.

It represents a total of 60 input strains. Fig. 16 presents the locations of the strain measurements used as input parameters on the cross patterns.

The output results were chosen to be the deflections and the twist angles at the locations of position transducers and inclinometers. It represents a total of 14 outputs.

The NN is composed of 60 neurons in the input layer, corresponding to the 60 input strain parameters, and one bias neuron. One hidden layer composed of one hundred neurons and one bias neuron was used. Increasing the number of hidden layers or changing the number of neurons in the hidden layer did not result in an improvement of the results. A 14 neuron output layer was used. Fig. 17 presents a schematic of the NN. The regularization term was set to 10 as it was the value giving the best results. The Adam solver was used.

For each monitored RST, the data were recorded for all the increment loads applied: from 10 to 100% and from 90 to 10% with 10% increments. The data were not recorded for RST1 at 10 and 20% during the increasing load phase.

The NN was trained for four cases. For each case, three RSTs, for all the applied loads, were used as a training set and the remaining RST, at an applied load of 100%, was used as the test set. A larger number of training load cases, not available in the present study, would ideally be used to train the model. For each case, the NN training was repeated 10 times and the optimized NN giving the highest coefficient of determination (R^2), when comparing the NN predictions to the experimental measurements, was selected. The highest R^2 obtained for each case are presented in Table 9. The worst overall predictions are made for RST2 and the best ones for RST4 with R^2 values of 0.737 and 0.991, respectively. RST3 predictions have a higher R^2 value than the ones for RST2, with values of 0.822 and 0.737, respectively. The computational time required to both train and test the NN was, for each case, around 3 s.

Fig. 18 presents the comparison between the predicted and the measured deflections along the front and rear spars. The discrepancies between predicted and measured deflections seem in accordance with the R^2 presented in Table 9: RST1 and RST4 shows the most accurate

Table 9
Highest R^2 obtained during the neural network training for each RST used as a test set.

	RST1	RST2	RST3	RST4
R^2	0.928	0.737	0.822	0.991

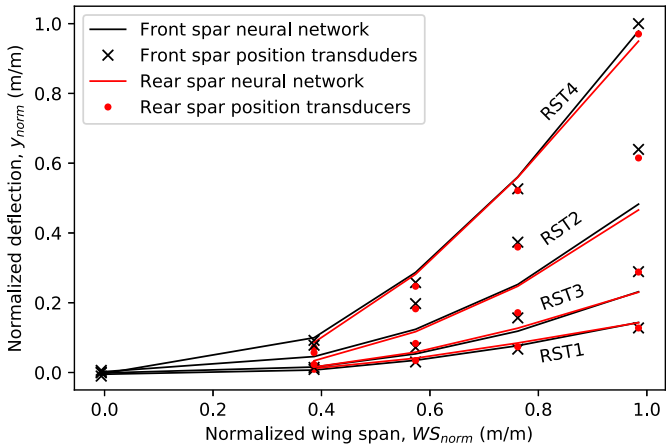

Fig. 18. Comparison between the neural network deflection predictions and the measurements derived from the position transducers for the front and rear spars. The neural network predictions are symbolized by straight lines linking the prediction points.

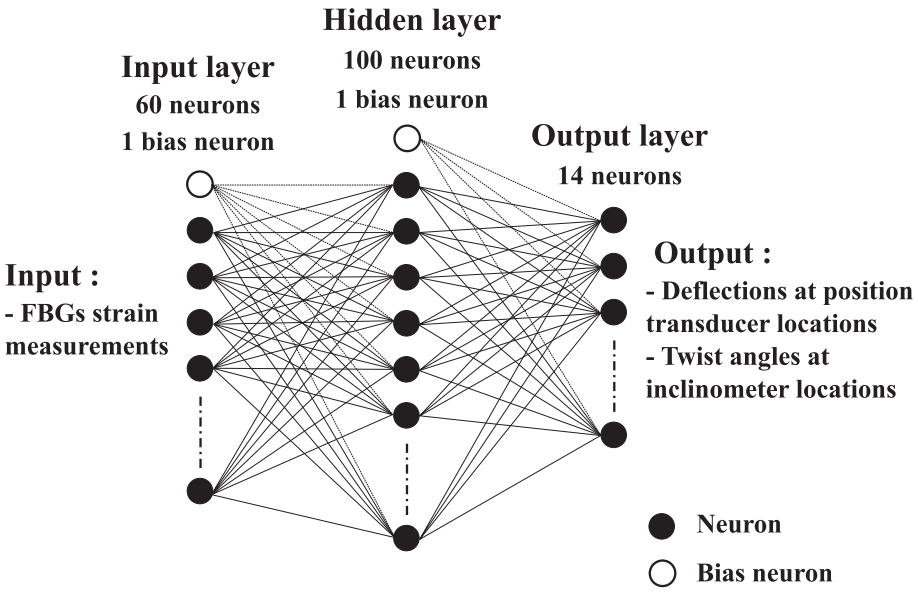

Fig. 17. Schematic of the neural network.

Table 10
Neural network predicted deflection percentage relative errors, y_{error}.

	Front spar, y_{error} (%)					Rear spar, y_{error} (%)			
	PT1	PT2	PT4	PT6	PT8	PT3	PT5	PT7	PT9
RST1	610.0	−18.86	16.0	14.7	12.2	26.8	19.8	15.1	12.0
RST2	−70.0	−41.6	−37.3	−32.4	−24.5	−40.8	−35.9	−31.2	−24.2
RST3	−85.5	6.97	−25.4	−24.3	−20.0	−32.7	−30.1	−26.0	−20.1
RST4	−436.8	8.2	11.3	6.5	−2.1	20.6	13.9	7.3	−2.1

predictions while RST2 shows the least accurate ones.

The neural network predictions relative errors, calculated using Equation (21), are presented in Table 10. The relative errors are all larger than the ones calculated with Meng's model (Tables 7 and 8). Indeed, the relative errors for RST1 to 3, in terms of absolute value, at the wing tip predicted with the NN are between 12 and 24.5% while they were between 0.3 and 2.0% when calculated with Meng's model. The rear and front spars relative errors predicted with the NN at the wing tip for RST4 are of −2.1%, which also represents a higher error than the results obtained with Meng's model (1.1% for both front and rear spars). The NN predictions show less accuracy than the results obtained with Meng's model. However, it should be recalled that more training loading cases should be used to properly train the NN. Thus, these results could likely be improved.

The errors on the twist angles predicted by the NN, calculated using Equation (24), are presented in Fig. 19. Except for RST2, all the predicted twist angles are in the error targeted range. The errors on the twist angle of RST2 for INC2 to 5 are out of the targeted range. Nevertheless, the RST2 NN twist angle predictions are better than the ones obtained using calculated and measured deflections (Fig. 14(b)) which were around 4 and 10°, respectively. Even though the number of training load cases is limited, the twist angles predicted by the NN are in the targeted error range, except for RST2, and are, for all cases, inferior to the ones obtained using the calculated and measured deflections. Thus, the NN can be considered as a promising method to develop for this purpose.

Increasing the number of load cases used in the training set should be considered as a future development. An option would be to use the results of a large number of load cases obtained by a wing FEM. These results could then be used to train a NN and simultaneously optimize the locations at which the FBGs should be installed. The deflections calculated using Meng's model or the Ko theory could also be used as input parameters. The NN could then be tested on experimental results obtained on a test rig. The load cases simulated using a FEM should be representative of what the structure will sustain (design or fatigue cases). If the FEM is linear, running unit cases for all directions and stations along wing span will represent all potential applied load configurations.

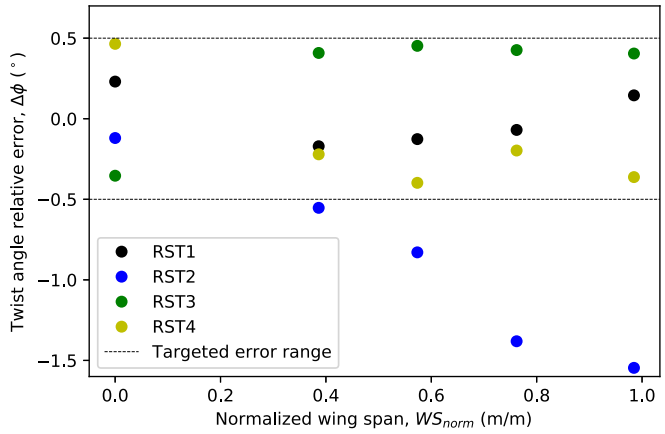

Fig. 19. NN predictions twist angle errors.

6. Conclusion

The left wing of the Global 7500 representative structure used to perform durability and damage tolerance testing (DADTT) was equipped with Fiber Bragg Gratings (FBG). The long-term objective was to develop a common method for both ground and flight tests to measure the deflection and the twist angle. Fatigue and static tests were monitored at the Bombardier Aviation Experimental department during certification tests. A comparison between the strain measurements obtained with FBGs and strain gauges was performed to validate the results obtained with FBGs. Front and rear spars deflections were analytically calculated. The wing twist angles were also calculated using both measured and calculated deflections. Finally, a prediction of the rear and front spars deflections and wing twist angles was made using a Neural Network (NN). The main conclusions are as follows:

- Meng's model and Ko theory were compared to a finite element beam bending model. Meng's model demonstrated more reliable prediction in the case of lacking data. It shall be noted that the actual Global 7500 DADTT has no strain data at the loading straps and access panels areas. Meng's model was thus chosen.
- Strain measured with FBGs were compared to the ones measured with strain gauges. Except for a few cases, the relative errors, for strain larger than 400 $\mu\varepsilon$, were in the range of ±5%. The larger errors observed might be attributable to large local strain gradients.
- The front spar deflection was calculated for a whole simulated flight with a relative error between −1 and 4%, at the wing tip, for medium and high amplitude deflections.
- The rear and front spars deflections during the static critical loading were calculated with relative errors between −1.9 and 2.0%. The relative deflection of the front spar, when compared to the one of the rear spar, was qualitatively predicted for all the studied load cases.
- The wing twist angles determined from the calculated and the measured deflections of the front and rear spars were, for all the monitored static critical load cases, out of the ±0.5° error targeted range at the wing tip. This method is not suitable to predict the wing twist angle.
- A NN was used to predict the wing deflections and twist angles during the static tests. The deflection predictions were less accurate than the ones calculated with Meng's model. However, the predicted twist angle errors were, except for one static test, within the ±0.5° targeted range for all the monitored static tests. These errors are smaller than those calculated using the deflections. It should be noted that the training sets used to feed the NN did not contain enough data and thus, the predictions could be enhanced.

This study shows that the NN is a promising method to predict the wing twist angle. The main challenge is to gather enough data representing enough different load cases to efficiently train the NN.

Future works could focus on using finite element models to obtain virtual strain measurements for a large number of different loading cases in order to efficiently train the NN. This data could also be used to optimize the locations at which the FBG should be installed. Finally, the agreement between experimental measurements and NN predictions should be studied. If successful, such a method would allow to indirectly measure the in-flight wing deflection and twist.

Declaration of competing interest

The authors declare that they have no known competing financial interests or personal relationships that could have appeared to influence the work reported in this paper.

Acknowledgements

This work was financially supported by Bombardier Aviation, CMC Electronics, Marinvent and the National Sciences and Engineering Research Council of Canada (NSERC) (grant number: RI-OPAIR-CCIP-488862).

References

[1] A.W. Burner, R.A. Wahls, W.K. Goad, Wing twist measurements at the national transonic facility, Tech. Rep. 110229 (1996). NASA.
[2] C.V. Jutte, W.L. Ko, C.A. Stephens, J.A. Bakalyar, W.L. Richards, Deformed Shape Calculation of a Full-scale Wing Using Fiber Optic Strain Data from a Ground Loads Test, 2011. Tech. Rep. NASA/TP-2011-215975, NASA, https://ntrs.nasa.gov/citations/20120004140.
[3] G.A. Fleming, H.L. Soto, B.W. South, S.M. Bartram, Advances in Projection Moiré Interferometry Development for Large Wind Tunnel Applications, 1999. Tech. Rep. 1999-01-5598, SAE Technical Paper, https://www.sae.org/publications/technical-papers/content/1999-01-5598/.
[4] T.E. Noll, J.M. Brown, M.E. Perez-Davis, S.D. Ishmael, G.C. Tiffany, M. Gaier, Investigation of the Helios Prototype Aircraft Mishap, 2004. Tech. rep. NASA, https://www.nasa.gov/pdf/64317main_helios.pdf.
[5] W.H. Bragg, W.L. Bragg, The reflection of x-rays by crystals, Proc. R. Soc. Lond. - Ser. A Contain. Pap. a Math. Phys. Character 88 (605) (1913) 428–438.
[6] K.O. Hill, G. Meltz, Fiber bragg grating technology fundamentals and overview, J. Lightwave Technol. 15 (8) (1997) 1263–1276.
[7] Z. Ma, X. Chen, Fiber bragg gratings sensors for aircraft wing shape measurement: recent applications and technical analysis, Sensors 19 (1) (2019) 55.
[8] A. Ghoshal, J. Ayers, M. Gurvich, M. Urban, N. Bordick, Experimental investigations in embedded sensing of composite components in aerospace vehicles, Compos. B Eng. 71 (2015) 52–62.
[9] H. Guo, G. Xiao, N. Mrad, J. Yao, Fiber optic sensors for structural health monitoring of air platforms, Sensors 11 (4) (2011) 3687–3705.
[10] G.C. Kahandawa, J. Epaarachchi, H. Wang, K. Lau, Use of fbg sensors for SHM in aerospace structures, Photonic Sensors 2 (3) (2012) 203–214.
[11] J.-R. Lee, C.-Y. Ryu, B.-Y. Koo, S.-G. Kang, C.-S. Hong, C.-G. Kim, In-flight health monitoring of a subscale wing using a fiber Bragg grating sensor system, Smart Mater. Struct. 12 (1) (2003) 147.
[12] W.L. Ko, W.L. Richards, V.T. Tran, Displacement Theories for In-flight Deformed Shape Predictions of Aerospace Structures, 2007. Tech. Rep. NASA/TP-2007-214612, NASA, https://ntrs.nasa.gov/citations/20070032936.
[13] W.L. Ko, W.L. Richards, Method for real-time structure shape-sensing, US Patent 7 (Apr. 21 2009) 520, 176.
[14] W.L. Ko, W.L. Richards, V.T. Fleischer, Applications of Ko Displacement Theory to the Deformed Shape Predictions of the Doubly-tapered Ikhana Wing, 2009. Tech. Rep. NASA/TP-2009-214652, NASA, https://ntrs.nasa.gov/citations/20090040594.
[15] J. Bakalyar, C. Jutte, Validation tests of fiber optic strain-based operational shape and load measurements, in: 53rd AIAA/ASME/ASCE/AHS/ASC Structures, Structural Dynamics and Materials Conference 20th AIAA/ASME/AHS Adaptive Structures Conference 14th AIAA, 2012, p. 1904.
[16] A. Derkevorkian, S.F. Masri, J. Alvarenga, H. Boussalis, J. Bakalyar, W.L. Richards, Strain-based deformation shape-estimation algorithm for control and monitoring applications, AIAA J. 51 (9) (2013) 2231–2240.
[17] M.J. Nicolas, R.W. Sullivan, W.L. Richards, Large scale applications using FBG sensors: determination of in-flight loads and shape of a composite aircraft wing, Aerospace 3 (3) (2016) 18.
[18] H. Li, L. Zhu, G. Sun, M. Dong, J. Qiao, Deflection monitoring of thin-walled wing spar subjected to bending load using multi-element FBG sensors, Optik 164 (2018) 691–700.
[19] Y. Meng, C. Xie, Z. Wan, Deformed wing shape prediction using fiber optic strain data, in: 17th International Forum on Aeroelasticity and Structural Dynamics vol. 4, IFASD, 2017, p. 2518, 2017.
[20] J. Yi, H. Zhang, X. Qiao, X. Zhu, Shape monitoring for wing structure using fiber Bragg grating sensors, in: IEEE 5th International Conference on Advanced Computational Intelligence (ICACI), IEEE, 2012, pp. 1032–1036, 2012.
[21] A. Tessler, J.L. Spangler, Inverse FEM for full-field reconstruction of elastic deformations in shear deformable plates and shells, Tech. Rep. 20040086696 (2004). NASA.
[22] A. Tessler, J.L. Spangler, A Variational Principle for Reconstruction of Elastic Deformations in Shear Deformable Plates and Shells, 2003. Tech. Rep. NASA/TM-2003-21445, NASA, https://ntrs.nasa.gov/citations/20030068121.
[23] A. Tessler, J.L. Spangler, A least-squares variational method for full-field reconstruction of elastic deformations in shear-deformable plates and shells, Comput. Methods Appl. Mech. Eng. 194 (2–5) (2005) 327–339.
[24] S.L. Vazquez, A. Tessler, C.C. Quach, E.G. Cooper, J. Parks, J.L. Spangler, Structural Health Monitoring Using High-Density Fiber Optic Strain Sensor and Inverse Finite Element Methods, 2005. Tech. Rep. NASA/TM-2005-213761, NASA, https://ntrs.nasa.gov/api/citations/20050185211/downloads/20050185211.pdf.
[25] X. Song, D. Liang, Dynamic displacement prediction of beam structures using fiber bragg grating sensors, Optik 158 (2018) 1410–1416.
[26] M. Gherlone, P. Cerracchio, M. Mattone, Shape sensing methods: review and experimental comparison on a wing-shaped plate, Prog. Aero. Sci. 99 (2018) 14–26.
[27] M. Gherlone, P. Cerracchio, M. Mattone, M. Di Sciuva, A. Tessler, Shape sensing of 3D frame structures using an inverse finite element method, Int. J. Solid Struct. 49 (22) (2012) 3100–3112.
[28] H. Murayama, K. Tachibana, Y. Hirano, H. Igawa, K. Kageyama, K. Uzawa, T. Nakamura, Distributed strain and load monitoring of 6 m composite wing structure by fbg arrays and long-length FBGs, in: OFS2012 22nd International Conference on Optical Fiber Sensors, vol. 8421, International Society for Optics and Photonics, 2012, p. 84212D.
[29] P. Cui, W. Zhang, Z. Wang, Y. Song, F. Li, Measurement of aircraft wing deformation using fiber Bragg gratings, in: 16th International Conference on Optical Communications and Networks (ICOCN), IEEE, 2017, pp. 1–3, 2017.
[30] A.T. Nguyen, J.-H. Han, A.T. Nguyen, Application of artificial neural networks to predict dynamic responses of wing structures due to atmospheric turbulence, International Journal of Aeronautical and Space Sciences 18 (3) (2017) 474–484.
[31] D. Wada, M. Tamayama, Wing load and angle of attack identification by integrating optical fiber sensing and neural network approach in wind tunnel test, Appl. Sci. 9 (7) (2019) 1461.
[32] M. Kaczmarek, A. Szymańska, Application of artificial neural networks to predict the deflections of reinforced concrete beams, Studia Geotechnica Mech. 38 (2) (2016) 37–46.
[33] B. Aviation, Global 7500 Bombardier Aviation, 2020 (accessed July 17, 2020)), https://businessaircraft.bombardier.com/fr/avions/global-7500#!#bba-pdp-section-5.
[34] C.A. Beltempo, A. Beaudoin, R. Pothier, Bombardier global 7500 fatigue test cycle rate commissioning to $^{1/4}$life, in: International Committee on Aeronautical Fatigue, Springer, 2019, pp. 708–722.